Acta Astronautica 151 (2018) 904–918

Contents lists available at ScienceDirect

Acta Astronautica

journal homepage: www.elsevier.com/locate/actaastro

Vibration suppression control of free-floating space robots with flexible appendages for autonomous target capturing

Deshan Meng[a,b], Weining Lu[a], Wenfu Xu[c], Yu She[b], Xueqian Wang[a,*], Bin Liang[a,**], Bo Yuan[a]

[a] Shenzhen Key Lab of Space Robotic Technology and Telescience, Graduate School at Shenzhen, Tsinghua University, Shenzhen, China
[b] Department of Mechanical and Aerospace Engineering, The Ohio State University, Columbus, USA
[c] Shenzhen Graduate School, Harbin Institute of Technology, Shenzhen, China

ARTICLE INFO

Keywords:
Space robot
Flexible appendage
Target capturing
Vibration suppression
Experiment system

ABSTRACT

Some flexible appendages, such as solar panels, communication antenna and other large structures are mounted on the base of the space robot. The structure flexibilities will cause vibration during the operation of manipulators. Due to complicated dynamic coupling among manipulators, the rigid base and flexible appendages, it is very challenging to control the end-effector to track inertial trajectories, especially when the target states are constantly changing. This paper proposes a vibration suppression method for autonomous target capturing during the preimpact phase without controlling the base. Firstly, we derive the rigid-flexible coupling dynamics of a space robot system with flexible appendages. Then, the relationship among joint rates, elastic motion and the end-effector velocities is established by using the linear momentum and angular momentum conservation equations. Secondly, a closed-loop control system is designed based on the dynamic coupling model. And the control system is composed of target motion prediction, autonomous trajectory planning, energy-based joint controllers and so on. Thirdly, the energy-based joint control is detailed, which is proved to be stable by Lyapunov direct method. Finally, simulations of a planar space robot with two flexible appendages and a 3D space robot with single flexible appendage are provided to verify the effectiveness of the presented approach. The effectiveness of energy-based joint control for vibration suppression is verified by a single-degree-of-freedom space robot experimental system. The simulation and experimental results show that the space manipulator can successfully capture the moving target while suppressing the structure vibration.

1. Introduction

Robotic systems are expected to play an increasingly important role in future space activities such as repairing, upgrading, refueling and re-orbiting spacecraft. The autonomous target capturing, which has been successfully demonstrated by the Engineering Test Satellite VII (ETS-VII) [1] and Orbital Express [2], is the key to on-orbit servicing. Some autonomous behaviors are necessary to perform complex and difficult tasks in space. Yoshida and Umetani developed on-line control scheme with vision feedback, using the Generalized Jacobian Matrix (GJM) concept for motion control and Guaranteed Workspace (GWS) for path planning [3]. Nagamatsu et al. designed a control system for the autonomous capture of a target satellite in space using a predictive trajectory based on the target satellite dynamics [4]. Xu et al. also proposed autonomous path planning and control methods to capture a noncooperative target based on the binocular stereo vision [5]. G Dong et al. [6] developed a hybrid approach based on adaptive extended Kalman filter and photogrammetry for the real-time pose and motion estimation of noncooperative targets. Benoit [7] presented a framework for autonomous capture operation of a non-cooperative mobile target in a 3-dimensional workspace using a robotic manipulator with visual servoing. The tracking and capture performance was improved significantly by using the Kalman filter. Huang et al. conducted a large number of studies on the capture of non-cooperative targets [8,9].

For the above works, the space robot is assumed to be a multi-rigid system. Actually, some flexible appendages [10,11] such as solar panels and communication antenna, will be mounted on the base of the space robot. For example, due to that large power is consumed to complete complex or long-term on-orbit servicing tasks, long solar arrays are mounted on the spacecraft. When a space robot with flexible appendages is deployed in space, structure flexibilities will easily cause vibration during orbit and/or attitude maneuvers of the base, and

* Corresponding author.
** Corresponding author.
E-mail addresses: wang.xq@sz.tsinghua.edu.cn (X. Wang), liangbin@tsinghua.edu.cn (B. Liang).

https://doi.org/10.1016/j.actaastro.2018.07.044
Received 18 December 2017; Received in revised form 14 July 2018; Accepted 22 July 2018
Available online 24 July 2018

operation of manipulators. Since there are little atmospheric damping in the orbit, the generated vibration will last a long time, even after the motion of the base and the manipulator stops. The modeling, planning and control of space robots with flexible appendages are very challenging. In the previous work, many scholars focused on flexible link or flexible joint manipulators [12–17]. Recently, some researchers devoted to study space robots with flexible appendages. Hirano et al. [18,19] developed a simple dynamic model of a space robot with a rigid manipulator and a flexible appendage, which was modeled using a virtual joint model. Kojima and Kasai [20,21] applied the input-shaping technique to control the link motion of a planar space robot equipped with single flexible appendage. Gasbarri and Pisculli [22] proposed a mixed NE/EL modeling formulation for a space robot with flexible solar arrays. Then two control strategies based on this dynamic model are addressed to compensate the structure vibrations. Zarafshan et al. [23] derived the dynamics model by virtually partitioning the whole system into rigid and flexible portions. An adaptive hybrid suppression control algorithm is then developed. For the controller design, the two portions are assembled together to form a proper model. Zhang et al. [24]studied a spatial dynamics and control of a 6-DOF space robot with flexible panels and the computed torque control method was used to design active controller to suppress the spacecraft drift caused by the impact. Xu et al. [25] developed a dynamic model and a closed-loop simulation system of a space robot with two flexible appendages for capturing large flexible spacecraft. Meng et al. [26] proposed a hybrid control method combining wave-based control and PD control to control the motion of a manipulator while suppressing the vibration of appendages.

Dubowsky and Torres [27,28] analyzed the dynamics behaviour between the base and the manipulator, then proposed the dynamic coupling map concept. Xu et al. [29,30] proposed the coupling factor to illustrate the motion and force dependencies and represent the degree of the dynamic coupling between the end-effector and the rigid base. Meng et al. [31] studied the dynamic coupling of space robots with flexible appendages and proposed a trajectory planning method to suppress structure vibration based on the coupling map. With flexible appendages, the dynamic behaviors of space robot become more complicated. The position and attitude of the end-effector will lose the desired values due to the structure vibration of flexible appendages [32]. It may cause the on-orbital task fails, even destroys the spacecraft. Thus, it is very important to control the vibration of flexible appendages. Due to the pose of target spacecraft changing from moment to moment, real-time autonomous adjustment is needed in the trajectory planning of space robots. For this reason, the methods applied to capture stationary targets such as off-line control and open-loop control, are not suitable for capturing moving targets.

In this paper, we focus on the vibration suppression control when space robots with flexible appendages automatically approach moving targets. For this purpose, a closed-loop control system of space robots is proposed to track the target trajectory while suppressing the vibration of the flexible appendages. Moreover, we design an energy-based joint control law for time-varying trajectories. The stability of the system is proved by Lyapunov direct method. Finally, we validate the proposed control method by simulation and experiment respectively.

The remainder of this paper is organised as follows. Section 2 establishes the dynamic and differential kinematic equations of a space robot with flexible appendages. In Section 3, we construct a closed-loop control system for autonomous target capturing. Section 4 details the energy-based joint control method for suppressing the structure vibration of flexible appendages. Section 5 presents simulation studies of typical cases using a 3-DOF planar space robot with two flexible solar paddles and a 7-DOF 3D space robot with a flexible appendage. In Section 6, we validate the effectiveness of the vibration control method using the space robot experiment system. The final section summarises and concludes the paper.

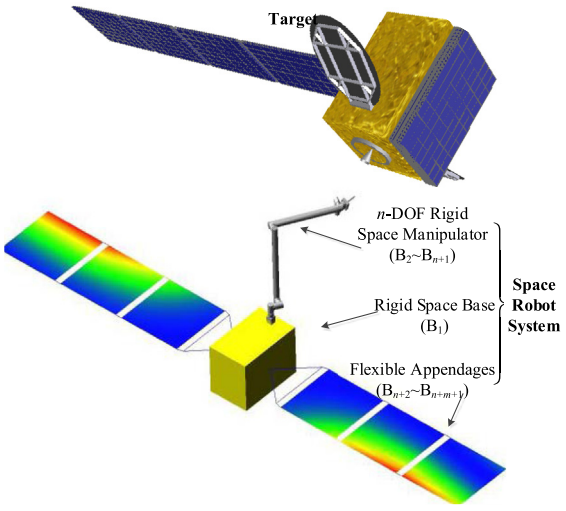

Fig. 1. The space robot system.

2. Modeling the space robot with flexible appendages

A common space robotic system with flexible appendages used for the on-orbit servicing mission is shown as Fig. 1.

It is composed of a central rigid body (called robot base), a serial manipulator (called space manipulator) with n degrees of freedoms (n DOFs), and m flexible appendages. Each flexible appendage is connected to the robot base through a rotating hinge with a degree of freedom. Hence, the space robot system can be described using ($n + m + 2$) bodies (including the inertial frame) and ($n + m + 1$) hinges.

2.1. Dynamics modeling of the space robot with flexible appendages

To derive the dynamics equations, the symbols (shown in Fig. 2) of the space robot with flexible appendages are defined. Σ_0, Σ_E are the inertia frame and the end-effector frame, respectively; Σ_i ($i = 1,\cdots, n+1$) is the body fixed frame of rigid body B_i; Σ_i ($i = n+2,\cdots, n+m+1$) is the floating frame of flexible body B_i; C_i ($i = 1, \ldots, n+1$) is the position of rigid body B_i's CM (center of mass); C_i ($i = n+2, \ldots, n+m+1$) is the position of flexible body B_i's CM; $\boldsymbol{r}_i \in \mathbf{R}^3$ ($i = 1, \ldots, n+1$) is the position vector of C_i; $\boldsymbol{r}_g \in \mathbf{R}^3$ is the position vector of the system's CM; $\boldsymbol{p}_e \in \mathbf{R}^3$ is the position vector of the end-effector; $\boldsymbol{a}_i \in \mathbf{R}^3$ ($i = 2, \ldots, n+1$) is the position vector from H_{i-1} to C_i; $\boldsymbol{b}_i \in \mathbf{R}^3$ ($i = 1, \ldots, n$) is the position vector from C_i to H_i; $\boldsymbol{b}_i \in \mathbf{R}^3$ ($i = n+1$) is the position vector from C_i to origin of Σ_E; $\boldsymbol{b}_i \in \mathbf{R}^3$ ($i = n+2, \ldots, n+m+1$) is the position vector from C_1 to H_i; $\boldsymbol{p}_i \in \mathbf{R}^3$ ($i = 2, \ldots, n+1$) is the position vector of H_i; $\boldsymbol{k}_i \in \mathbf{R}^3$ ($i = 2, \ldots, n+1$) is unit vector representing the rotation direction of H_i; $\Theta \in \mathbf{R}^n$ is the manipulator joint angle vector, i.e. $\Theta = [\theta_2 \cdots \theta_{n+1}]^T$; $\Psi_1 \in \mathbf{R}^3$ is the base attitude represented by x-y-z Euler angles; $\dot{\mathbf{x}}_b \in \mathbf{R}^6$ is the linear velocity and angular velocity of B_0, i.e. $\dot{\mathbf{x}}_b = [\mathbf{v}_1^T \ \ \boldsymbol{\omega}_1^T]^T$; $\dot{\mathbf{x}}_e \in \mathbf{R}^6$ is the linear velocity and angular velocity of the end-effector, i.e. $\dot{\mathbf{x}}_e = [\mathbf{v}_e^T \ \ \boldsymbol{\omega}_e^T]^T$. It should be pointed out that, a vector is generally written as ${}^j\boldsymbol{r}_b$, where, the left superscript "j" denotes the frame in which the vector is described. When it denotes the inertia frame, the left superscript can be deleted.

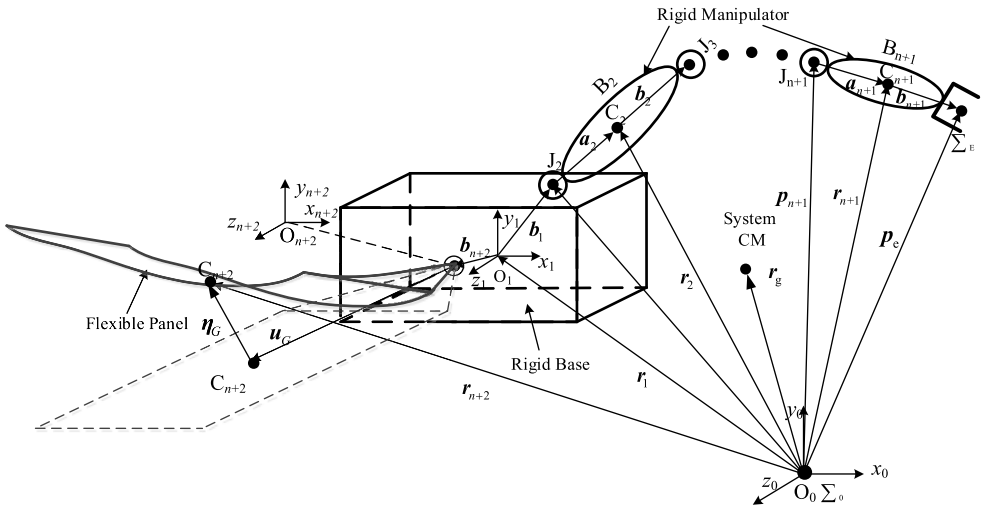

Fig. 2. The model of the space robot with flexible appendages.

As is shown in Fig. 3, the inertial position of any point P of the flexible body B_i is:

$$\mathbf{s}_P = \mathbf{r}_1 + \mathbf{b}_i + \mathbf{u}_P + \boldsymbol{\eta}_P \quad (i = n+2, \ldots, n+m+1) \tag{1}$$

where $\boldsymbol{u}_P$ is the position vector of point P (which coincides with point p for the undeformed configuration) from point O_i, $\boldsymbol{\eta}_P$ is a measure of elastic displacement. O_i is the origin of the floating coordinate system of the flexible body B_i. $\boldsymbol{u}_P$ and $\boldsymbol{\eta}_P$ are described in the inertial frame.

$$\boldsymbol{\eta}_P = \mathbf{A}_i {}^i\boldsymbol{\eta}_P \tag{2}$$

Matrix $\boldsymbol{A}_i$ represents the orientation of the floating frame of flexible body B_i with respect to the inertial frame. The elastic displacement ${}^i\boldsymbol{\eta}_P$ can be represented as a linear combination of the deformation modes of flexible body B_i as

$${}^i\boldsymbol{\eta}_P(x, y, z, t) = \boldsymbol{\varphi}\boldsymbol{\xi}(t) = \sum_{j=1}^{s_i} \boldsymbol{\varphi}_j \boldsymbol{\xi}_j \tag{3}$$

The modal matrix $\boldsymbol{\varphi}$ is a constant matrix which can be obtained by the structure dynamics analysis using the finite element method. $\boldsymbol{\xi}_j$ ($j = 1, \cdots, s_i$) is the elastic displacement coordinates of flexible body B_i. And s_i is the number of modal coordinate for flexible body B_i.

The dynamic equation of the compounded system with flexible appendages is as follows [25]:

$$\begin{bmatrix} \mathbf{H}_{bb} & \mathbf{H}_{b\theta} & \mathbf{H}_{b\xi} \\ \mathbf{H}_{b\theta}^T & \mathbf{H}_{\theta\theta} & \mathbf{H}_{\theta\xi} \\ \mathbf{H}_{b\xi}^T & \mathbf{H}_{\theta\xi}^T & \mathbf{H}_{\xi\xi} \end{bmatrix} \begin{bmatrix} \ddot{\mathbf{x}}_b \\ \ddot{\boldsymbol{\Theta}} \\ \ddot{\boldsymbol{\xi}} \end{bmatrix} + \mathbf{C}(\mathbf{x}_b, \boldsymbol{\Theta}, \boldsymbol{\xi}, \dot{\mathbf{x}}_b, \dot{\boldsymbol{\Theta}}, \dot{\boldsymbol{\xi}}) \begin{bmatrix} \dot{\mathbf{x}}_b \\ \dot{\boldsymbol{\Theta}} \\ \dot{\boldsymbol{\xi}} \end{bmatrix} + \begin{bmatrix} 0 & 0 & \\ & & \mathbf{K}_\xi \end{bmatrix} \begin{bmatrix} \mathbf{x}_b \\ \boldsymbol{\Theta} \\ \boldsymbol{\xi} \end{bmatrix} = \begin{bmatrix} 0 \\ \boldsymbol{\tau}_m \\ 0 \end{bmatrix} \tag{4}$$

In the equation above, $\boldsymbol{H}_{bb}$, $\boldsymbol{H}_{b\theta}$, $\boldsymbol{H}_{b\xi}$, $\boldsymbol{H}_{\theta\theta}$, $\boldsymbol{H}_{\theta\xi}$ and $\boldsymbol{H}_{\xi\xi}$ denote sub-mass matrices. $\boldsymbol{C}$ ($\boldsymbol{x}_b$, Θ, $\boldsymbol{\xi}$, $\dot{\mathbf{x}}_b$, $\dot{\boldsymbol{\Theta}}$, $\dot{\boldsymbol{\xi}}$) denotes the coupling matrix including Coriolis force and centrifugal force. Additionally, $\boldsymbol{K}_\varphi$ denotes the stiffness matrix of the flexible appendages, and $\boldsymbol{\tau}_m \in \mathbf{R}^n$ is a vector composed of the driving torques of the manipulator joints.

2.2. Differential kinematics in free-floating mode

The kinematic equation of the end-effector of the space robot with flexible appendages is as follows:

$$\begin{bmatrix} \mathbf{v}_e \\ \boldsymbol{\omega}_e \end{bmatrix} = \mathbf{J}_b \begin{bmatrix} \mathbf{v}_1 \\ \boldsymbol{\omega}_1 \end{bmatrix} + \mathbf{J}_m \dot{\boldsymbol{\Theta}} \tag{5}$$

where, $\boldsymbol{v}_e \in \mathbf{R}^3$ and $\boldsymbol{\omega}_e \in \mathbf{R}^3$ are respectively the linear and angular velocities of end-effector with respect to the inertial frame. $\boldsymbol{J}_b \in \mathbf{R}^{6\times 6}$ is the Jacobian matrix dependent on the base motion and $\boldsymbol{J}_m \in \mathbf{R}^{6\times n}$ is the Jacobian matrix dependent on the manipulator motion.

$$\mathbf{J}_b = \begin{pmatrix} \mathbf{E} & -\tilde{\mathbf{p}}_{1e} \\ \mathbf{O} & \mathbf{E} \end{pmatrix} \in R^{6\times 6}, \quad \mathbf{p}_{1e} = \mathbf{p}_e - \mathbf{r}_1 \tag{6}$$

$$\mathbf{J}_m = \begin{bmatrix} \mathbf{k}_2 \times (\mathbf{p}_e - \mathbf{p}_2) & \cdots & \mathbf{k}_{n+1} \times (\mathbf{p}_e - \mathbf{p}_{n+1}) \\ \mathbf{k}_2 & \cdots & \mathbf{k}_{n+1} \end{bmatrix} \in \mathbf{R}^{6\times n} \tag{7}$$

To facilitate description, the generalized variables of the system are combined as follows:

$$\mathbf{y} = [\mathbf{x}_b, \boldsymbol{\Theta}, \boldsymbol{\xi}]^T \tag{8}$$

Assuming that the system is initially motionless and no external forces/torques act on the system, the following relationship holds on:

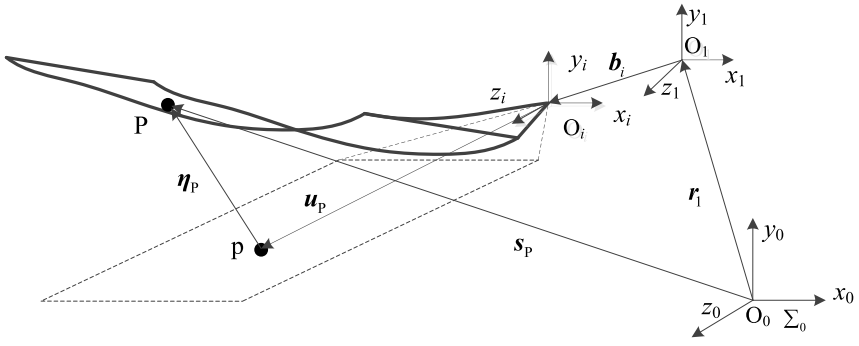

Fig. 3. The flexible appendage B_i.

$$\mathbf{H}_{bb}\dot{\mathbf{x}}_b + \mathbf{H}_{b\theta}\dot{\boldsymbol{\Theta}} + \mathbf{H}_{b\xi}\dot{\boldsymbol{\xi}} = 0 \tag{9}$$

According to equation (9), $\dot{\mathbf{x}}_b$ can be solved as follows:

$$\dot{\mathbf{x}}_b = -\mathbf{H}_{bb}^{-1}\mathbf{H}_{b\theta}\dot{\boldsymbol{\Theta}} - \mathbf{H}_{bb}^{-1}\mathbf{H}_{b\xi}\dot{\boldsymbol{\xi}} \tag{10}$$

Substituting equation (10) into (5), the following relationship is given:

$$\dot{\mathbf{x}}_e = \mathbf{J}_g\dot{\boldsymbol{\Theta}} + \mathbf{J}_\xi\dot{\boldsymbol{\xi}} \tag{11}$$

where,

$$\mathbf{J}_g = \mathbf{J}_m - \mathbf{J}_b\mathbf{H}_{bb}^{-1}\mathbf{H}_{b\theta} \in R^{6\times n} \tag{12}$$

$$\mathbf{J}_\xi = -\mathbf{J}_b\mathbf{H}_{bb}^{-1}\mathbf{H}_{b\xi} \in R^{6\times s} \tag{13}$$

In above equations, $\boldsymbol{J}_g$ is the so-called Generalized Jacobian Matrix (GJM) [33]. It represents the dynamic interaction between the joint motion and the end-effector motion. $\boldsymbol{J}_\xi$ represents the dynamic interaction between the appendage elastic motion and the end-effector motion. In this paper, $\boldsymbol{J}_g$ and $\boldsymbol{J}_\xi$ are called Generalized Rigid Jacobian Matrix and Generalized Flexible Jacobian Matrix, respectively.

3. The closed-loop control for autonomous target capturing

The target capture process includes three specific phases: the preimpact phase, the contact/impact phase and the post-impact phase. During the preimpact phase, the space manipulator's end-effector tracks and approaches the target spacecraft to its capturing box. In the impact phase, the contact/impact between the manipulator hand and the object is established, and a force impulse is generated. After the space robot captures the target successfully (i.e., post-impact phase), a compounded system is formed, which includes the space robot and the grasped target. In this paper, we focus on researching the vibration suppression of flexible appendages during the preimpact phase.

3.1. The closed-loop control framework

The whole closed-loop control system used during the preimpact phase is mainly composed of four modules (shown in Fig. 4): Relative pose measurement and target motion prediction, Autonomous trajectory planning, Energy-based vibration suppression controller and Dynamic model. The main processes of autonomous target capturing are shown in Fig. 4 as following:

(1) Set the stopping criteria, i.e. position error ε_p, orientation error ε_o, and the allowed maximal time t_{max};
(2) Measure the pose of the handle of the target relative to the end-effector. Get the pose error (i.e. ep, eo), and judge whether the target is within the capturing box (i.e. the grasp area, $||ep|| \le \varepsilon p$ and $||eo|| \le \varepsilon o$). If so, the manipulator closes its gripper and grasps the target; else, go to step 3;
(3) Autonomous trajectory planning includes two sub-steps:
  (a) Plan velocities of the end-effector, and drive the end-effector to track and approach the target along the shortest path (i.e. straight line);
  (b) Calculate the desired joint rates $\dot{\boldsymbol{\Theta}}_d$ with the autonomous singularity avoiding. Then the desired joint angle $\boldsymbol{\Theta}_d$ is determined by integrating $\dot{\boldsymbol{\Theta}}_d$;
(4) Generate the driving torques of the manipulator joints based on energy-based joint control to follow $\boldsymbol{\Theta}_d$ and $\dot{\boldsymbol{\Theta}}_d$, simultaneously suppress the vibration of flexible appendages. The joint control law will be detailed in Section 4.
(5) $t = t + \Delta t$, if $t < t_{max}$, go to step 2; else, the algorithm stops, which means the space robot can't capture the target in the prescribed time, i.e. this capture failed.

3.2. Target motion predicting

The relative position is provided by cameras mounted on the end-effector and represented by the following formula:

$$\mathbf{e}_p = \mathbf{p}_{et} = \mathbf{p}_t - \mathbf{p}_e \tag{14}$$

where, $\boldsymbol{p}_e$ represents the position of the origin of the end-effector coordinate system in the inertial coordinate system; $\boldsymbol{p}_t$ represents the position of the origin of the target handle coordinate system in the inertial coordinate system.

The relative attitude angle measured by hand-eye camera is the handle coordinate system relative to the end-effector coordinate system. It can be represented by the following formula:

$$\mathbf{e}_o = \boldsymbol{\Psi}_t - \boldsymbol{\Psi}_e \tag{15}$$

where, Ψ_t is the posture of the handle coordinate system relative to the inertial coordinate system; Ψ_e is the posture of the end-effector coordinate system relative to the inertial coordinate system.

The target motion state can be estimated using the Kalman filter or other similar methods [6,7] and it is not studied in this article. We suppose that the motion velocities of the target are known, and the linear velocity and angular velocity of the target are defined as $\boldsymbol{v}_t$ and $\boldsymbol{\omega}_t$ respectively.

3.3. Autonomous trajectory planning

3.3.1. End-effector velocity planning

The desired velocities of the end-effector are calculated with

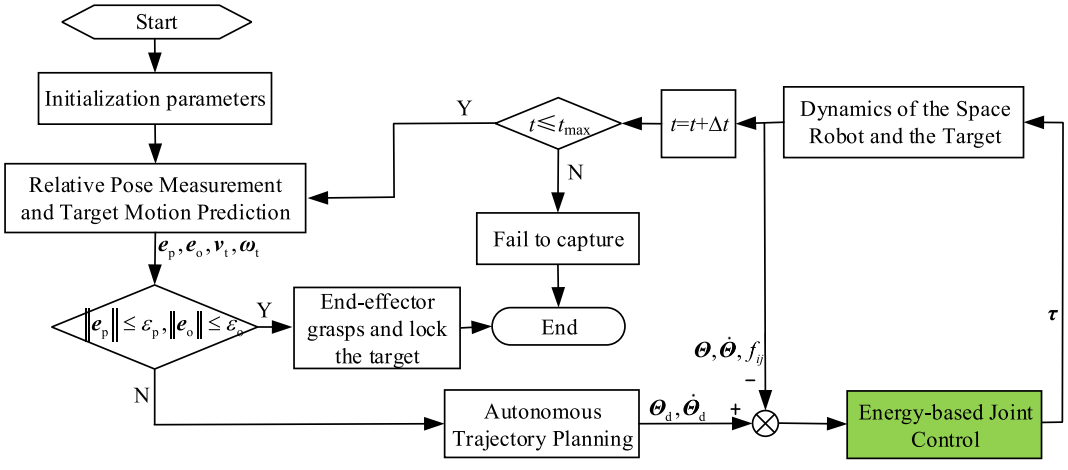

Fig. 4. The architecture of closed-loop control system during the preimpact phase.

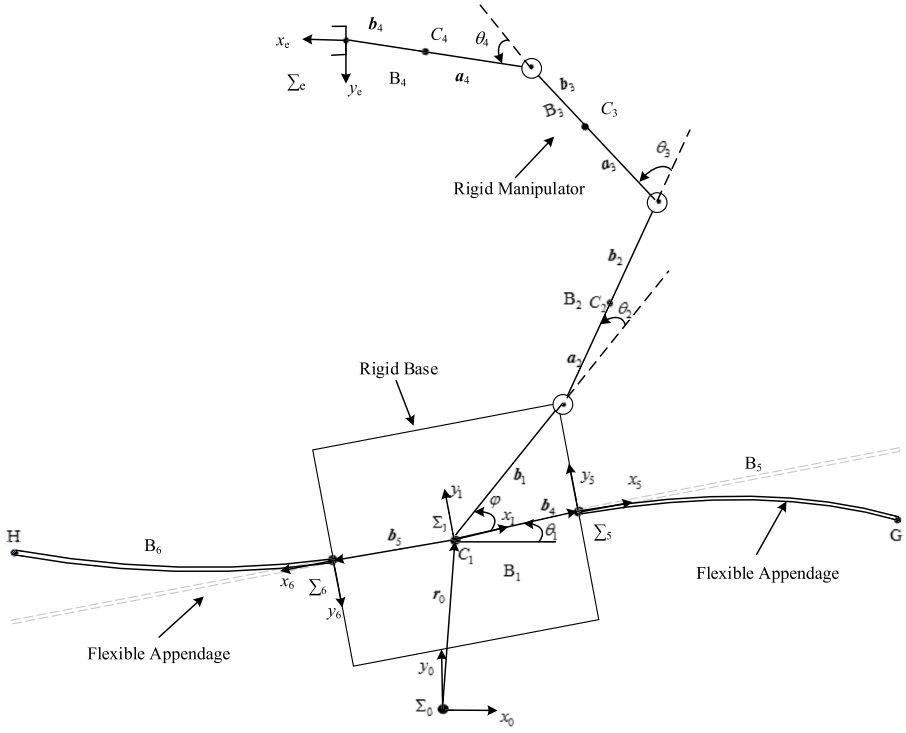

Fig. 5. A 3-DOF planar space robot with two flexible solar paddles.

Table 1
Mass parameters of rigid bodies.

Parameters	Rigid body				
	B_1	B_2	B_3	B_4	Target
m (kg)	1530	30	30	60	5000
$\mathbf{a}_i$(m)	0	1.15	1.15	0.2	–
	0	0	0	0	–
$\mathbf{b}_i$(m)	0.882	1.15	1.15	0.64	–
	0.297	0	0	0	–
$\mathbf{I}_i(kg{\cdot}m^2)$	177.16	2	2	7.41	900

proportional - differential form:

$$\begin{cases} \mathbf{v}_{ed} = \mathbf{K}_{pv}\mathbf{e}_p + \mathbf{K}_{vv}\mathbf{v}_t \\ \boldsymbol{\omega}_{ed} = \mathbf{N}_{Euler}(\boldsymbol{\Psi}_e)\mathbf{K}_{p\omega}\mathbf{e}_o + \mathbf{K}_{v\omega}\boldsymbol{\omega}_t \end{cases} \tag{16}$$

where, $\boldsymbol{K}_{pv}$, $\boldsymbol{K}_{p\omega}$ are proportional coefficients, the values of them limit the velocity of end-effector. $\boldsymbol{K}_{vv}$, $\boldsymbol{K}_{v\omega}$ are differential coefficients. $\boldsymbol{N}_{\text{Euler}}$ (Ψ_e) is the transformation matrix for transforming the time derivation of Euler angles to the attitude angular velocity.

To avoid excessive velocity of the end-effector, the following constraints are adopted:

$$\mathbf{v}_{ed} = \begin{cases} \frac{v_{em}}{|\mathbf{v}_{ed}|}\mathbf{v}_{ed}, & \text{if } |\mathbf{v}_{ed}| \geq v_{em} \\ \mathbf{v}_{ed}, & \text{else} \end{cases} \tag{17}$$

$$\boldsymbol{\omega}_{ed} = \begin{cases} \frac{\omega_{em}}{|\boldsymbol{\omega}_{ed}|}\boldsymbol{\omega}_{ed}, & \text{if } |\boldsymbol{\omega}_{ed}| \geq \omega_{em} \\ \boldsymbol{\omega}_{ed}, & \text{else} \end{cases} \tag{18}$$

where, v_{em}, ω_{em} are the maximum allowable linear velocity and the maximum allowable angular velocity of the end-effector respectively. The values of coefficients mentioned in equation (16) are used to limit the velocity of the end-effector. After the velocity of the end-effector is constrained by formulas (17) and (18), the values of these coefficients can be taken as $\boldsymbol{K}_{pv} = \boldsymbol{K}_{vv} = \boldsymbol{K}_{p\omega} = \boldsymbol{K}_{v\omega} = \text{diag}\ [1,1,1]$.

Table 2
The control parameters.

Trajectory tracking control	Vibration suppression control
$k_{p2} = k_{p3} = k_{p4} = 0.01$ $k_{d2} = k_{d3} = k_{d4} = 1600$	$\alpha_2 = \alpha_3 = \alpha_4 = 50000$ $\beta_2 = \beta_3 = \beta_4 = 0.1$

3.3.2. Joint motion planning

The kinematics equation of the space robot with flexible appendages in free-floating mode is given in (11). Considering the modal coordinates are uncontrolled, the desired angular velocity of joints can be calculated as following:

$$\dot{\boldsymbol{\Theta}}_d = \mathbf{J}_g^{-1}\hat{\dot{x}}_{ed} \tag{19}$$

where, $\dot{\boldsymbol{\Theta}}_d$ is the desired angular velocity of the manipulator joint. $\hat{\dot{x}}_{ed}$ is the desired motion of the end-effector after vibration compensation, $\hat{\dot{x}}_{ed} = \dot{\mathbf{x}}_{ed} - \mathbf{J}_\xi\dot{\boldsymbol{\xi}}$.

The influence of vibration on the joints velocity planning can be eliminated through the compensation mentioned above [32]. But it is difficult to obtain the modal variables. And this influence can be cut down only by reducing the value of $\mathbf{J}_\xi\dot{\boldsymbol{\xi}}$ in actual engineering applications. Thus, the vibration suppression of flexible appendages is necessary during autonomous target capturing.

The singularities of $\boldsymbol{J}_g$ exist in most workspace. Dynamic singularity is functions of the system mass properties and cannot be predicted from its kinematics. Thus, in this paper a damped least-squares method [34] is adopted to avoid dynamic singularity. Replace $(\boldsymbol{J}_g)^{-1}$ by $(\boldsymbol{J}_g)^{\#}$:

$$\dot{\boldsymbol{\Theta}}_d = \mathbf{J}_g{}^{\#}\dot{\mathbf{x}}_{ed} \tag{20}$$

where, $(\boldsymbol{J}_g)^{\#}$ is the minimum variance inverse of the Jacobian matrix.

$$\mathbf{J}_g{}^{\#} = (\mathbf{J}_g{}^T\mathbf{J}_g + \lambda^2\mathbf{I})^{-1}\mathbf{J}_g{}^T \tag{21}$$

In equation (21), λ is damping coefficient and can adaptively adjust it's value as following:

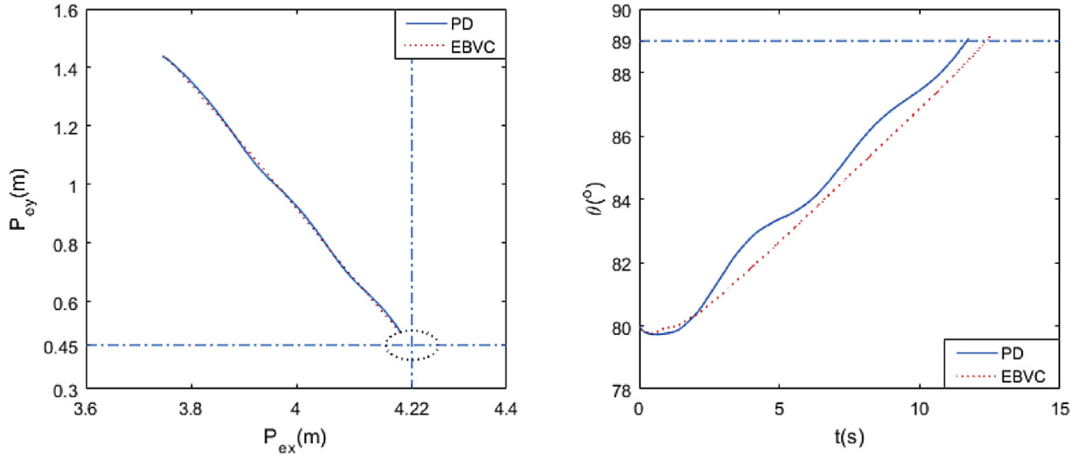

Fig. 6. The trajectory of the manipulator end-effector.

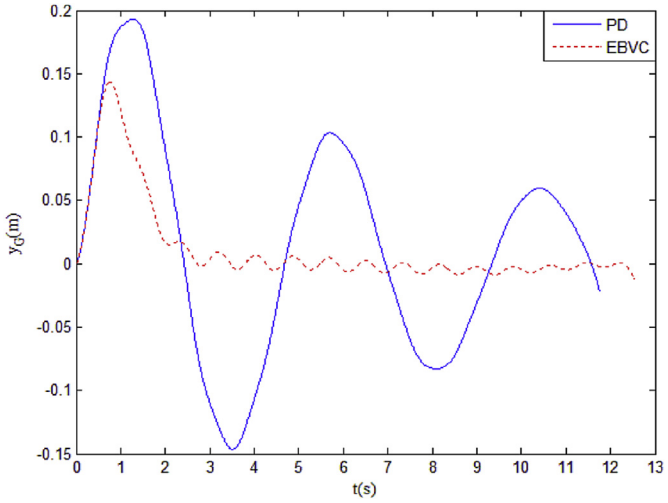

Fig. 7. The vibration curve of solar panel at point G.

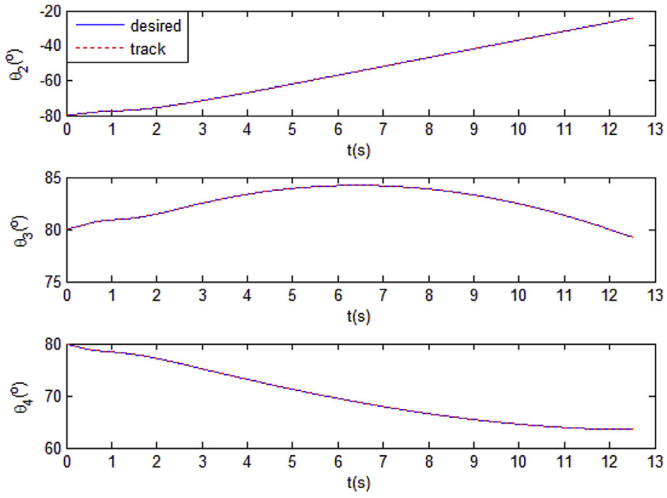

Fig. 9. The curves of the joint angles.

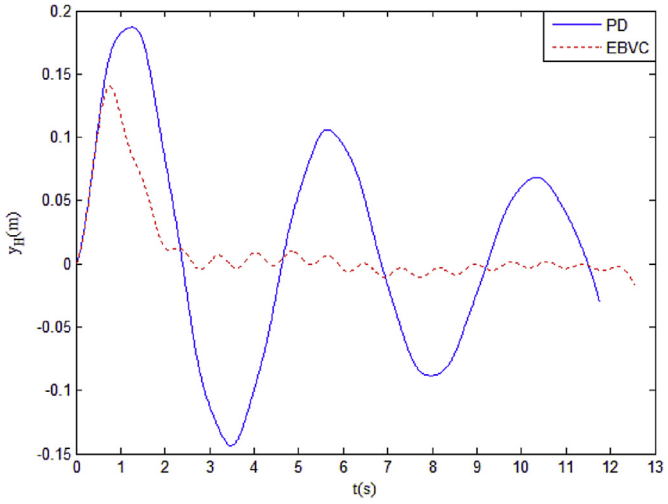

Fig. 8. The vibration curve of solar panel at point H.

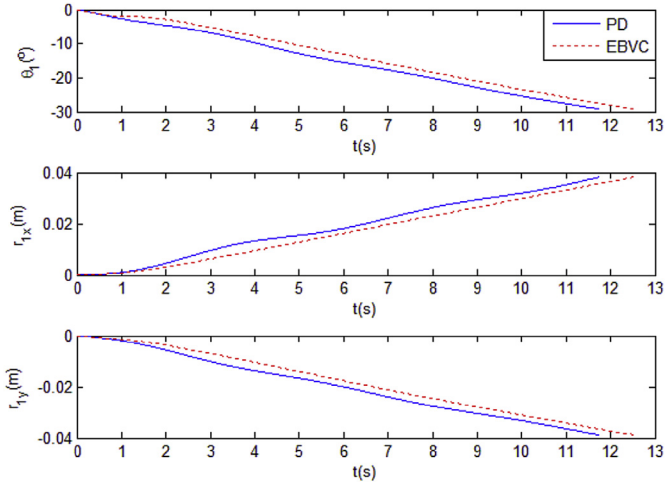

Fig. 10. The pose of the space robot base.

$$\lambda^2 = \begin{cases} 0, & \text{if } \hat{\sigma}_n \geq \varepsilon \\ \left(1 - \left(\frac{\hat{\sigma}_n}{\varepsilon}\right)^2\right)\lambda_m^2, & \text{other} \end{cases} \tag{22}$$

where, $\hat{\sigma}_n$ is the estimated value of the minimum singular value; ε is the threshold to judge the singularity; λ_m is the maximum damping value.

In order to prevent the excessive angular velocities of the joint, the angular velocity of the joint is limited as following:

$$\dot{\theta}_{id} = \begin{cases} \frac{\dot{\theta}_{im}}{|\dot{\theta}_{id}|}\dot{\theta}_{id}, & \text{if } |\dot{\theta}_{id}| \geq \dot{\theta}_{im} \\ \dot{\theta}_{id}, & \text{else} \end{cases} \quad (i = 1,2,\ldots,n) \tag{23}$$

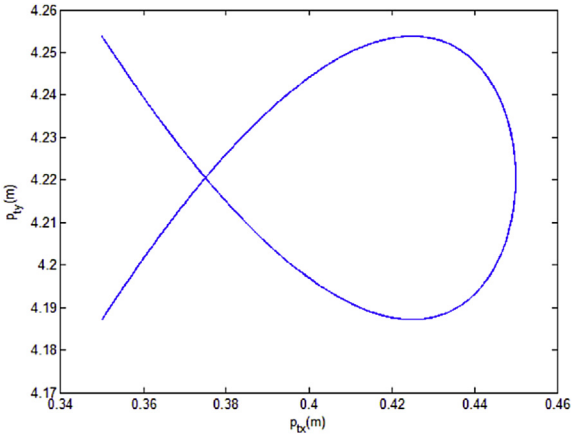

Fig. 11. The target displacement curve.

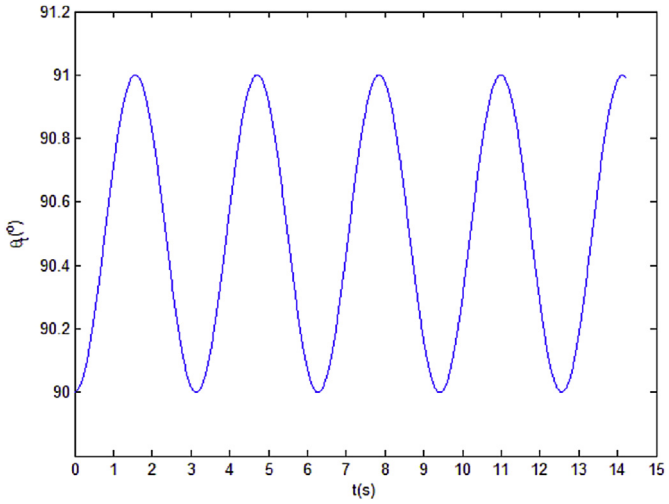

Fig. 12. The posture changing of target.

Table 3
The control parameters.

Trajectory tracking control	Vibration suppression control
$k_{p1} = k_{p2} = k_{p3} = 2000$ $k_{d1} = k_{d2} = k_{d3} = 160$	$\alpha_1 = \alpha_2 = \alpha_3 = 50000$ $\beta_1 = \beta_2 = \beta_3 = 0.1$

The desired joint angles are obtained by integrating the joint angular velocity:

$$\boldsymbol{\Theta}_d = \boldsymbol{\Theta} + \dot{\boldsymbol{\Theta}}_d \Delta t \tag{24}$$

After the desired joint angle and angular velocity are gotten, the driving torques of the manipulator joint can be calculated by the energy-based vibration suppression controller proposed in section 4. Then, the driving torques are used in the dynamic equation (4) to get the states of the space robot system in the next moment.

4. Energy-based joint control for vibration suppression

For a free-floating space robot with flexible appendages, the motion of the space manipulator will cause vibration of flexible appendages under the effect of dynamic coupling. Similarly, the vibration of flexible appendages can be eliminated by control of the space manipulator. The aim of this control scheme is ensuring a good trajectory tracking of the manipulator and suppressing vibrations of flexible appendages. In Refs. [35,36] an energy-based control method is studied for flexible links and

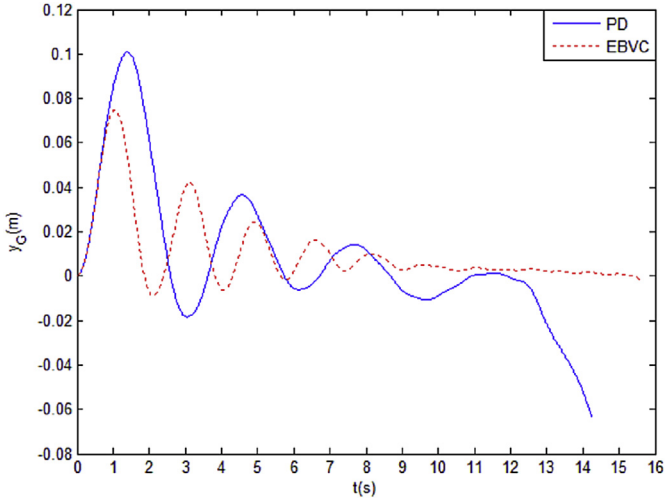

Fig. 13. The vibration curve of solar panel at point G.

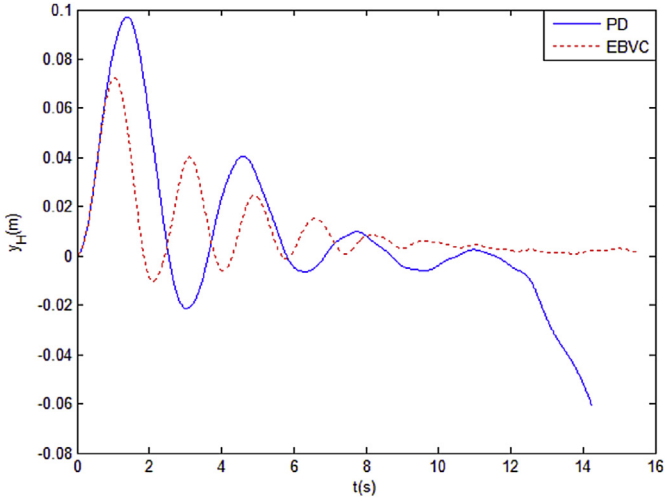

Fig. 14. The vibration curve of solar panel at point H.

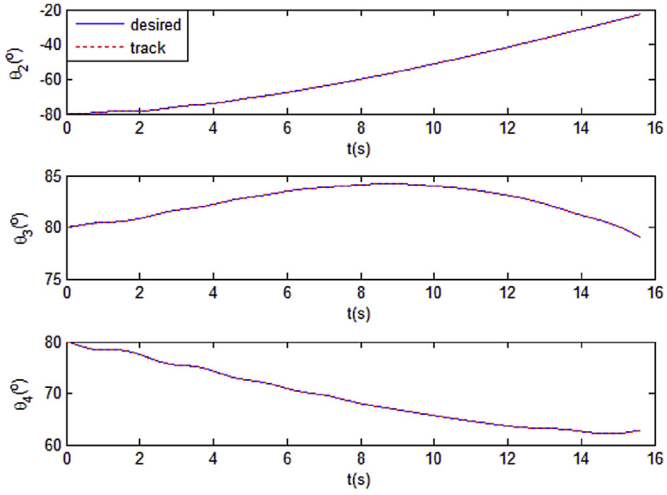

Fig. 15. The curves of the joint angles.

only suitable for tracking the constant desired joint angles. In this paper, an energy-based controller is designed to solve the vibration suppression for tracking time-varying desired joint angles.

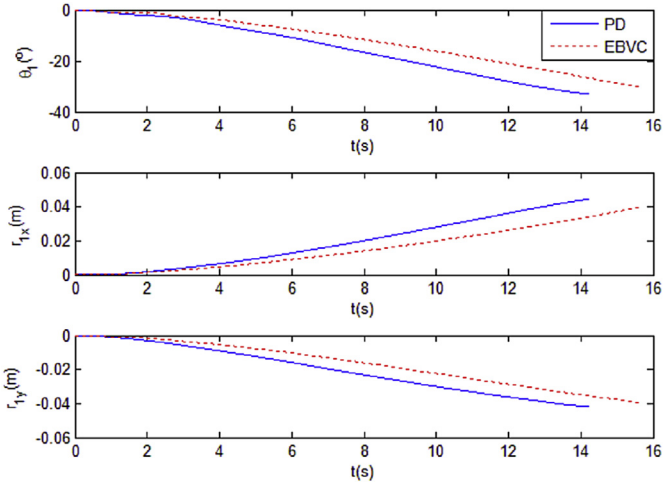

Fig. 16. The pose of the space robot base.

4.1. Joint control law

The adaptive controller that provides the joint torques is described by the following law:

$$\tau_i = k_{pi}e_i(t) + k_{di}\dot{e}_i(t) - \sum_{j=n+2}^{n+m+1} k_{ij}(t)f_{ij}(t) \quad (i = 2,...,n+1; j = n+2,...,n+m+1) \tag{25}$$

where k_{pi} and k_{di} are positive constant parameters for the $(i\text{-}1)^{th}$ manipulator joint; $e_i(t)$ and $\dot{e}_i(t)$ represent the error in the joint angle and velocity for the $(i\text{-}1)^{th}$ link as follows:

$$e_i(t) = \theta_{di}(t) - \theta_i(t) \tag{26}$$

In equation (25), $k_{ij}(t)$ is a time-varying parameter and is calculated by the following formula:

$$\dot{k}_{ij}(t) = \alpha_i f_{ij}(t)\dot{\theta}_i(t) - \beta_i k_{ij}(t) - \frac{\alpha_i k_{pi}}{k_{ij}(t)}e_i(t)\dot{\theta}_{di}(t) - \frac{\alpha_i k_{di}}{k_{ij}(t)}\dot{e}_i(t)\dot{\theta}_i(t) \tag{27}$$

where, α_i and β_i are positive parameters. From equation (27) we can know that $k_{ij}(t)$ depends on $\theta_{di}(t)$、 $\dot{\theta}_{di}(t)$、 $\theta_i(t)$、 $\dot{\theta}_i(t)$ and $f_{ij}(t)$. To avoid that $k_{ij}(t)$ is too large to cause the joint torque beyond acceptable range, the term $-\beta_i k_{ij}$ is introduced to prevent this problem [35]. In addition, the boundary values of $k_{ij}(t)$ are also defined as $[-k_{ij\max}, -k_{ij\min}]\cup[k_{ij\min}, k_{ij\max}]$. $k_{ij}(t)$ takes boundary values when it is beyond borders. Obviously, k_{ijmin} requires greater than zero.

In equations (25) and (27), $f_{ij}(t)$ is any combination of feedback signals relating to vibrations of the jth flexible appendage. The condition to choose $f_{ij}(t)$ is that they must be zero when the jth flexible appendage undergoes no deformation. Hence, the elastic displacement or the strain of any point P of the flexible appendage can be chosen as $f_{ij}(t)$. In this paper, the y-axis position of point P expressed in the floating coordinate system of the flexible body B_j (as shown in Fig. 3) is chosen as $f_{ij}(t)$,

$$f_{ij}(t) = y({}^j\boldsymbol{\eta}_P) \tag{28}$$

4.2. Stability analysis

Since the gravity can be ignored in the space, there are only kinetic energy (denoted by E_k) and elastic potential energy (denoted by E_p) for the space robot with flexible appendages. If the damping and friction of the space robot system are ignored, the total change of the energy of the free-floating space robot system is equal to the total work done by the manipulator joint motor torque, i.e.:

$$E_k(t) + E_p(t) - E_k(0) - E_p(0) = \sum_{i=2}^{n+1}\int_0^t \tau_i\dot{\theta}_i dt \tag{29}$$

where, $E_k(t)$ and $E_p(t)$ are the total kinetic energy and the elastic potential energy of the whole system at time t. $E_k(0)$ and $E_p(0)$ are initial kinetic energy and initial potential energy of the whole system. By taking the time derivative of both sides of equation (29), we can get

$$\dot{E}_k(t) + \dot{E}_p(t) = \sum_{i=2}^{n+1}\tau_i\dot{\theta}_i \tag{30}$$

The Lyapunov function is defined as follows:

$$V(t) = E_k(t) + E_p(t) + \frac{1}{2}\sum_{i=2}^{n+1}k_{pi}(\theta_{di}(t) - \theta_i(t))^2 + \frac{1}{2}\sum_{i=2}^{n+1}\sum_{j=n+2}^{n+m+1}\frac{k_{ij}^2(t)}{\alpha_i} \tag{31}$$

The derivative of $V(t)$ is then:

$$\dot{V}(t) = \dot{E}_k(t) + \dot{E}_p(t) + \sum_{i=2}^{n+1}k_{pi}(\theta_{di}(t) - \theta_i(t))(\dot{\theta}_{di}(t) - \dot{\theta}_i(t)) + \sum_{i=2}^{n+1}\sum_{j=n+2}^{n+m+1}\frac{k_{sj}(t)\dot{k}_{sj}(t)}{\alpha_i} \tag{32}$$

Substituting equation (30) into equation (32), the following equation is obtained:

$$\dot{V}(t) = \sum_{i=2}^{n+1}\tau_i\dot{\theta}_i + \sum_{i=2}^{n+1}k_{pi}(\theta_{di} - \theta_i)(\dot{\theta}_{di} - \dot{\theta}_i) + \sum_{i=2}^{n+1}\sum_{j=n+2}^{n+m+1}\frac{k_{sj}\dot{k}_{sj}}{\alpha_i} \tag{33}$$

Substituting the control law (25) and equation (27) into equation (33), the following result is obtained:

$$\dot{V}(t) = -\sum_{i=2}^{n+1}\sum_{j=n+2}^{n+m+1}\frac{\beta_i}{\alpha_i}k_{ij}^2(t) \tag{34}$$

Equation (34) shows $\dot{V}(t)$ is negative semi-definite. It implies that

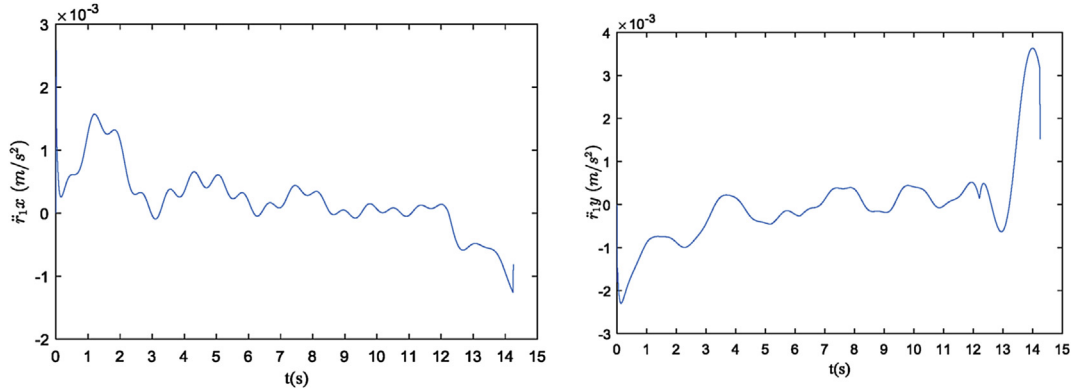

Fig. 17. The accelerations of the space robot base using PD control.

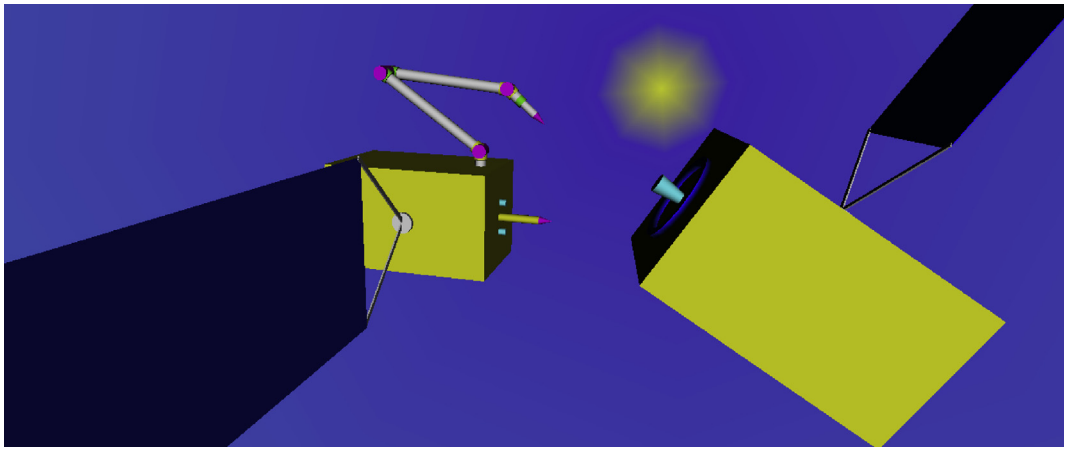

Fig. 18. The 3D space robot system and the target.

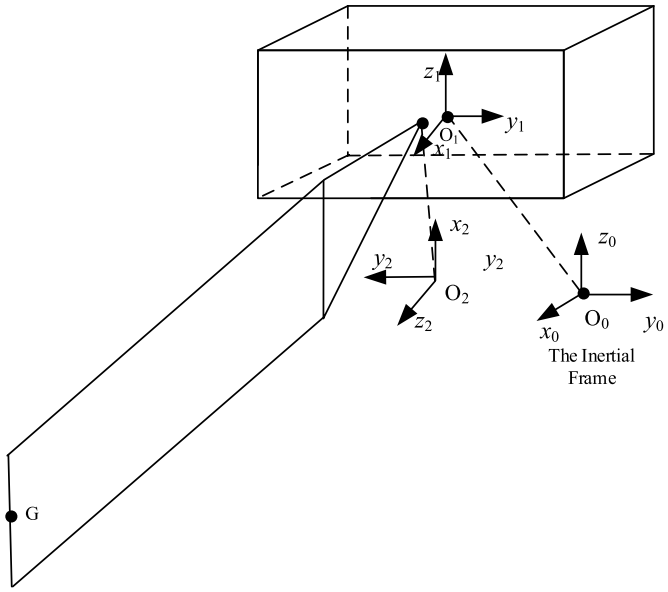

Fig. 19. The coordinate system of the space base and its solar wing.

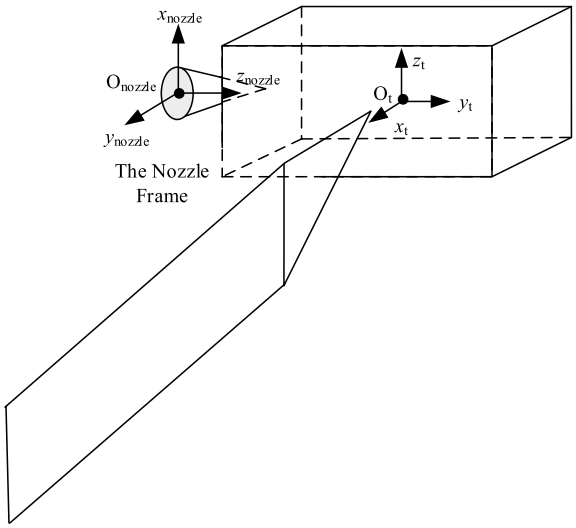

Fig. 20. The coordinate system of the target spacecraft.

the energy along the system trajectories can't increase. The controlled system is energy dissipative. Then, the proposed control law (25) can guarantee the stability of the closed-loop control system of space robot with flexible appendages.

5. Simulation study

5.1. A planar space robot system with flexible appendages

A 3-link planar space robot with two flexible appendages is taken as a practical example to verify the proposed method. It is composed of a 3-DOF rigid manipulator, a rigid base and two flexible appendages, shown in Fig. 5. The parameters of the flexible appendages are as follows: the length is $l_5 = l_6 = 3.5$ m; the linear density is 10 kg/m; the bending stiffness is EI = 175 kg m^2. The flexible appendage of space robot (i.e. bodies B_5 and B_6) are respectively installed at [0.75 m, 0 m] and [-0.75 m, 0 m] with respect to the body frame of B_1. The mass parameters of rigid bodies are shown in Table 1.

Initially, the position of the base centroid and the attitude angle of the base are both zero. And the joint angles of the space manipulator are assumed to be:

$$\boldsymbol{\Theta}_0 = [-80^o,\ \ 80^o,\ \ 80^o]^T \tag{35}$$

The pose of the target coordinate system is as follows:

$$\mathbf{r}_{t0} = [4.22\ \ 0.45]^T \tag{36}$$

$$\theta_{t0} = 90^o \tag{37}$$

The proposed vibration suppression control of flexible appendages during autonomous target capturing is verified based on the simulation of typical cases. In order to show the effectiveness of the proposed control strategy, the simulations results using traditional PD controller are also given to compare with the proposed method.

Actually, by setting $k_{ij}(t) \equiv 0$, the energy-based joint control law given in equation (25) will be reduced to the traditional PD controller, i.e.:

$$\tau_i = k_{pi}(\theta_{di} - \theta_i) + k_{di}(\dot{\theta}_{di} - \dot{\theta}_i)\ \ (i = 2,3,4) \tag{38}$$

5.1.1. Stationary target capturing simulation

The control parameters used in the simulation are shown in Table 2. The simulation results are shown in Figs. 6–10. Fig. 6 shows the pose of the manipulator end-effector. The target is successfully captured when

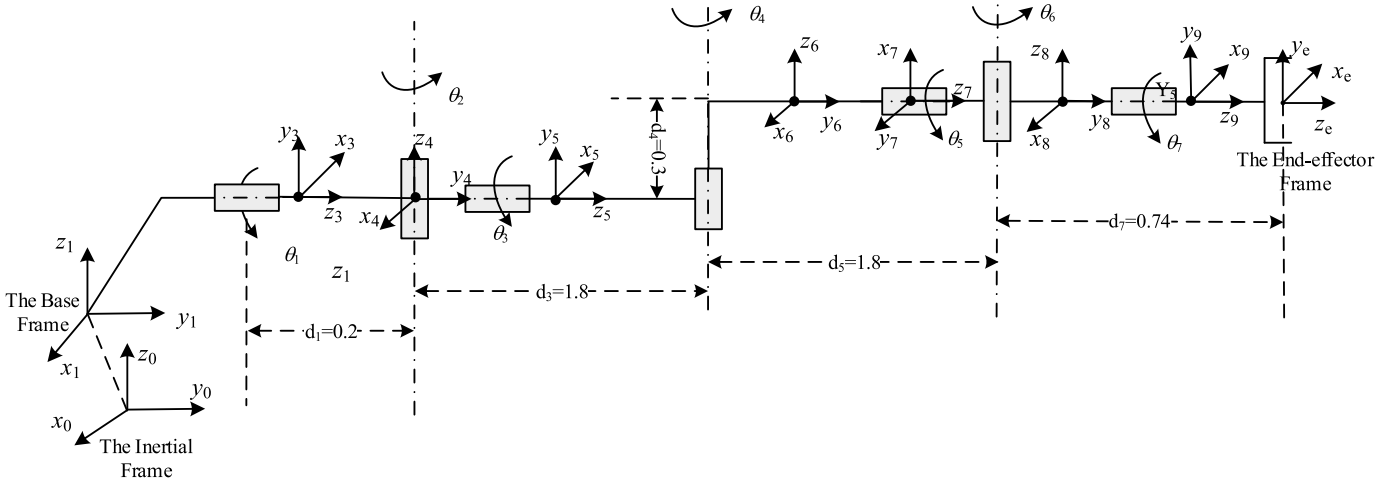

Fig. 21. The coordinate system of the space robot.

Table 4
The geometric and material parameters of the solar wing.

Parameter	Size $a \times b \times c$ (m)	Density ρ(kg/m^3)	Elastic modulus E (Pa)	Poisson's ratio υ
	16.262 × 2.29 × 0.025	30	8×10^9	0.3

$t_f = 12.52s$ by using the EBVC (energy-based vibration suppression control) method.

Figs. 7 and 8 show the vibration curves of the flexible wings. The vibration of the solar wings is described by using the movement displacement of the end point of the solar wing relative to the y-axis direction of the floating coordinate system. Figs. 7 and 8 respectively illustrate the vibrations (i.e., the y-axis position of Point G and Point H) of solar wing B_5 and B_6. It can be seen that the vibration level of B_5 and B_6 resulted by using EBVC method is significantly lower than that by using the PD controller. Taking B_5 as an example, the maximum amplitude of the B_5 reaches 193 mm by using the PD controller, but it is only 143 mm by using EBVC method. The vibration amplitude decays rapidly to less than 10 mm after $t = 3s$ in the case of using EBVC method. However when using the PD controller, the vibration amplitude is still up to 60 mm at $t = 10.4s$.

Fig. 9 shows tracking curves and planning curves of joint angles by using EBVC method. The results show that the EBVC method can implement the expected goals and has very good performance. The pose of the robot base is shown in Fig. 10. For the PD control, the attitude and the centroid position of the base vary from 0° to 29.1° and from [0 m, 0 m]^T to [0.0382 m, −0.0388 m]^T, respectively. And they are from 0° to −29.2° and from [0 m, 0 m]^T to [0.0382 m, −0.0387 m]^T for the EBVC control. The results show that changes of base's pose are essentially identical for the two control methods.

5.1.2. Moving target capturing simulation

Another case for simulation is moving target capturing. The moving speed of the target is as follows:

$$\mathbf{v}_t = [-100\sin(2t) \quad 100\sin(2t)]^T \text{ mm/}s \tag{39}$$

$$\omega_t = \sin(2t)^o/s \tag{40}$$

where, $\boldsymbol{v}_t$ and ω_t are respectively the linear velocity and angular velocity of the target. The centroid position and attitude of the target are shown in Fig. 11 and Fig. 12 respectively. The control parameters are listed in Table 3.

The simulation results are shown in Figs. 13–16. Fig. 13 and Fig. 14 show the vibration curves of the flexible wings. It can be also seen that the vibration levels of B_5 and B_6 by using EBVC method are significantly lower than those by using PD controller. Taking B_5 as an example, the maximum vibration amplitude of B_5 reaches 100 mm by using PD controller, but it is only 74 mm by using EBVC method. For the PD control, the final vibration value is −63 mm. But it is only −2.8 mm for the EBVC control, and it satisfies the grasp condition.

Fig. 15 shows tracking curves and planning curves of joint angles by using EBVC method. And the results also show that the EBVC method can implement the desired goals and has very good performance for moving target capturing. The pose of the robot base is shown in Fig. 16. For the PD control, the attitude and the centroid position of the base vary from 0° to −33° and from [0 m, 0 m]^T to [0.045 m, −0.042 m]^T, respectively. And they are from 0° to −30.2° and from [0 m, 0 m]^T to [0.039 m, −0.039 m]^T for the EBVC control. Fig. 17 shows the accelerations of the space robot base by using PD control. The results show that a sudden increase of the accelerations of the space robot base after 12s stimulates the flexible appendages to generate large vibrations.

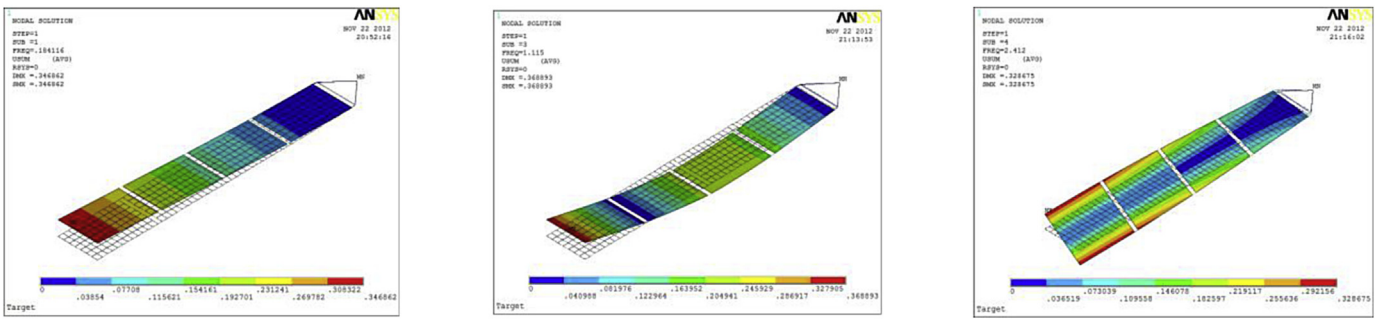

Fig. 22. The first three order vibration modes of the solar wing.

Table 5
The mass properties of rigid bodies.

		B_1	B_2	B_3	B_4	B_5	B_6	B_7	B_8	target
Mass (kg)		1500	11.08	12	18	10	18	12	14.08	5000
$\boldsymbol{a}_i$ (m)		0	0	0	0	0	0	0	0	–
		0	0	0	0	−0.9	0	−0.1	0	–
		0	−0.1	0	−0.9	−0.3	0	0	0	–
$\boldsymbol{b}_i$ (m)		0	0	0	0	0	0	0	0	–
		0.9	0	0	0	0.9	0	0.1	0	–
		0.75	0.1	0	0.9	0	0	0	0.54	–
$\boldsymbol{I}$(Kg·m^2)	I_{xx}	800	0.0505	0.0547	4.8850	0.2207	4.8850	0.0547	0.0505	1000
	I_{yy}	600	0.0505	0.0547	4.8850	0.2207	4.8850	0.0547	0.0505	800
	I_{zz}	700	0.0272	0.0294	0.0441	0.0245	0.0441	0.0294	0.0272	900
	I_{xy}	0	0	0	0	0	0	0	0	0
	I_{yz}	0	0	0	0	0	0	0	0	0
	I_{xz}	0	0	0	0	0	0	0	0	0

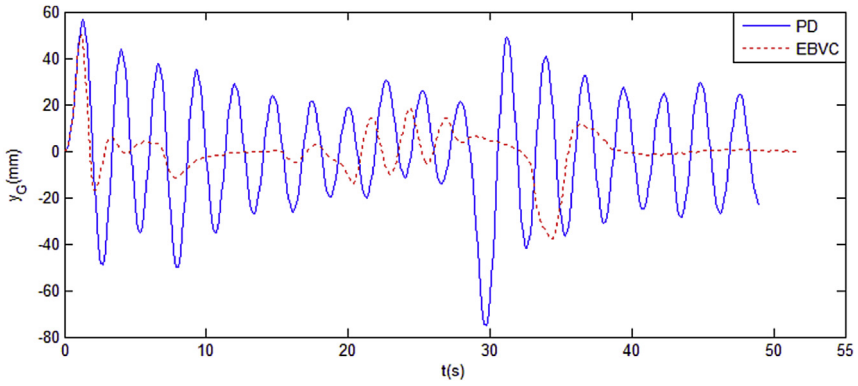

Fig. 23. The vibration curve of solar panel at point G.

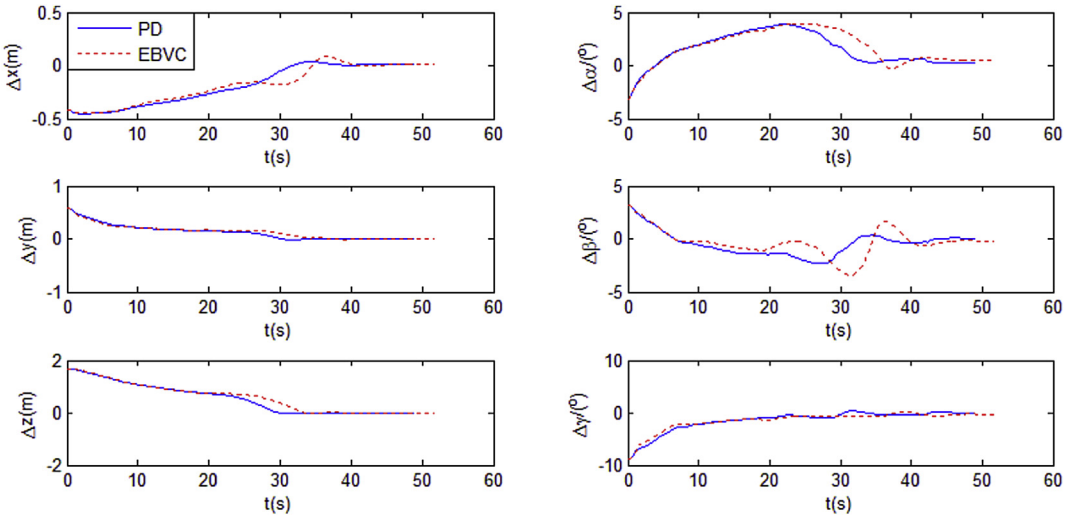

Fig. 24. The curves of relative pose for capturing moving target.

5.2. A 3D space robot system with a flexible appendage

The designed space robot system (shown in Fig. 18) used for the simulation is composed of a central rigid body, a flexible solar panel and a 7-DOF serial manipulator. The solar paddle is connected to the robot base through a rotating hinge with one degree of freedom. Hence, the space robot can be described using 10 bodies (including the inertial frame) and 9 hinges.

5.2.1. The model parameters

The space robot is a hybrid rigid-flexible system, i.e. it is composed of rigid and flexible bodies. The centroid frame and floating coordinate system are respectively used as the body-fixed frames of the rigid and flexible bodies. Fig. 19 shows the coordinate systems for the robot base and its solar wing. Frame $O_1x_1y_1z_1$is the centroid frame of B_1. The origin is located in the center of mass (CM) of B_1. Frame $O_2x_2y_2z_2$ is the floating coordinate system of B_2 (it is a flexible body). Its origin, i.e. O_2, is located at the hinge between the solar paddle (B_2) and the central rigid body B_1. The body-fixed frames of the space manipulator are defined as Fig. 21 (when the joint angles are all zero). The origins are located in the centroid of each link of the manipulator. The z-axes of the frames are the rotation directions of corresponding joints. The coordinate systems of the target spacecraft are shown in Fig. 20, where, $O_tx_ty_tz_t$ is the centroid frame of target. A frame, denoted as

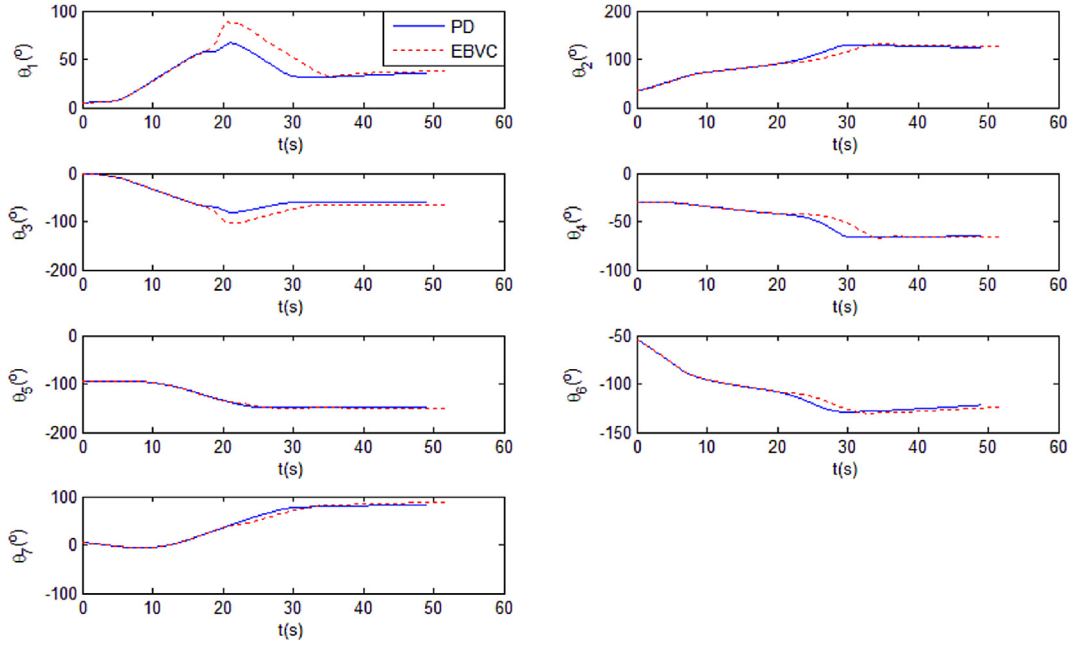

Fig. 25. The curves of the joint angles.

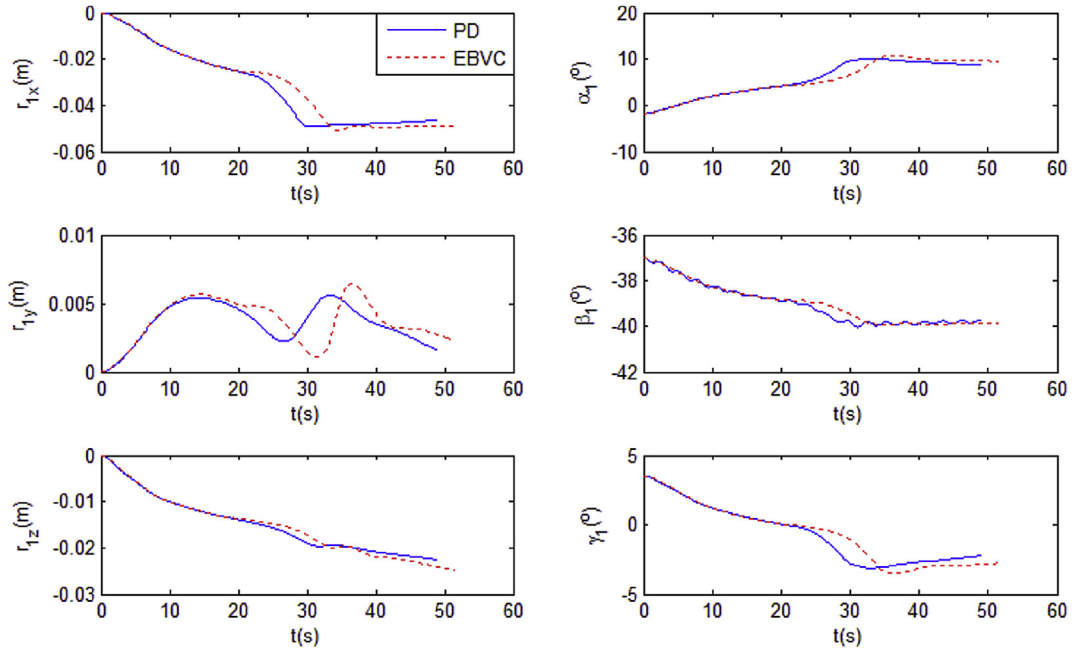

Fig. 26. The pose of the space robot base.

$x_{nozzle}y_{nozzle}z_{nozzle}$, is defined to represent the apogee engine nozzle. Its origin is located in the circle center of the bottom surface of the apogee engine nozzle. And the position of the origin relative to the centroid frame of target is [0 m, −2.29 m, 0 m]. For the capturing simulation, the nozzle frame is taken as the target frame of visual measurement and navigation algorithm for the space robot.

The solar wing of the space robot (i.e., bodies B_2) is installed at [0.75 m, 0 m, 0 m] with respect to the centroid frame of B_1. The geometric and material parameters of the solar wing are shown in Table 4.

With structural modal analysis of the solar wing by ANSYS software, we can get the natural frequencies, the modal matrixes, the lumped mass of each node, the position vector from the origin of the floating reference frame to each node, etc. These parameters are used for the simulation. The first three natural frequencies calculated by ANSYS are 0.1841 Hz, 1.1154 Hz and 2.4119 Hz, respectively. And the first three order vibration modes of the solar wing are shown in Fig. 22.

The mass properties of rigid bodies in the space robot are listed in Table 5.

5.2.2. *Moving target capturing simulation*

The initial positions of the chaser's CM and the target's CM relative to the inertial frame are respectively:

$$\mathbf{r}_{I0} = [0 \quad 0 \quad 0]^{\mathrm{T}}\mathrm{m} \tag{41}$$

$$\mathbf{r}_{t0} = [4.5 \quad 0.05 \quad 2.8]^{\mathrm{T}}\mathrm{m} \tag{42}$$

The attitudes of the chaser and the target are respectively:

$$\boldsymbol{\Psi}_{I0} = [-1.8^{\circ} \quad -37^{\circ} \quad 3.5^{\circ}]^{\mathrm{T}} \tag{43}$$

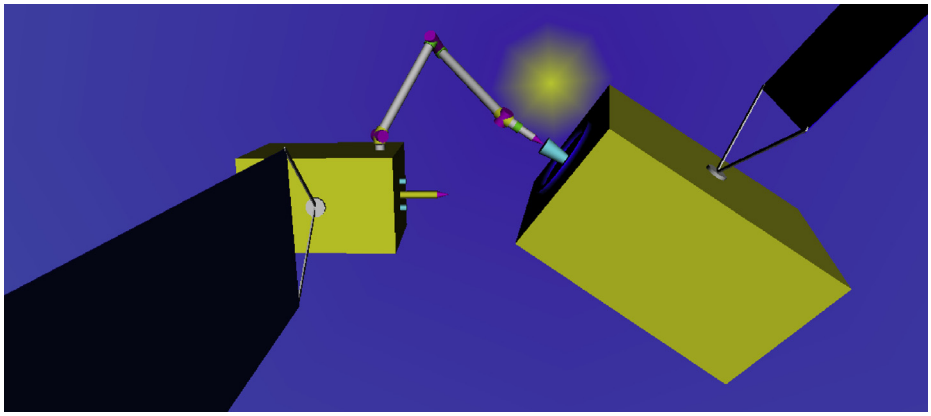

Fig. 27. The final state after capturing moving target.

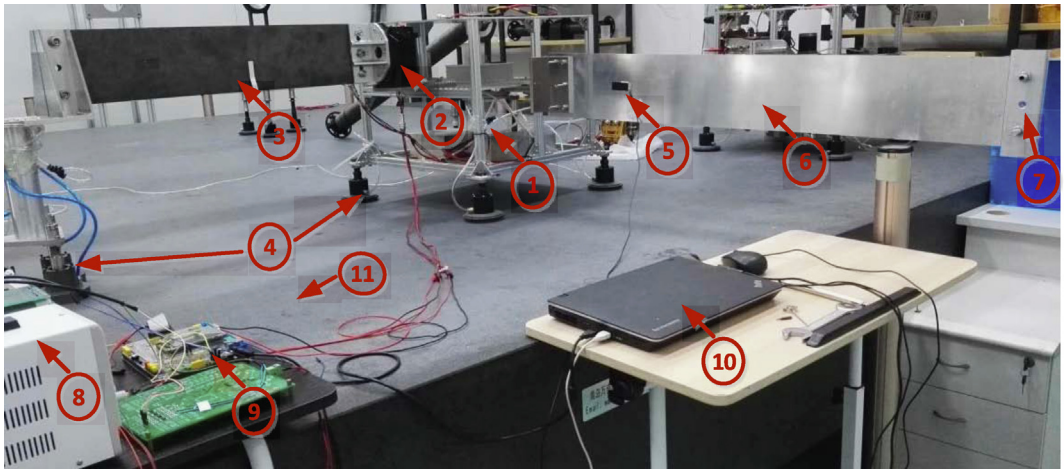

Fig. 28. The experiment setup of vibration test: 1. Space robot base, 2. Joint, 3. Steel plate, 4. Air feet, 5. Piezoelectric sensor, 6. Aluminum plate, 7. Aluminum block, 8. Power supply, 9. Central control unit, 10. PC, 11. Marble platform.

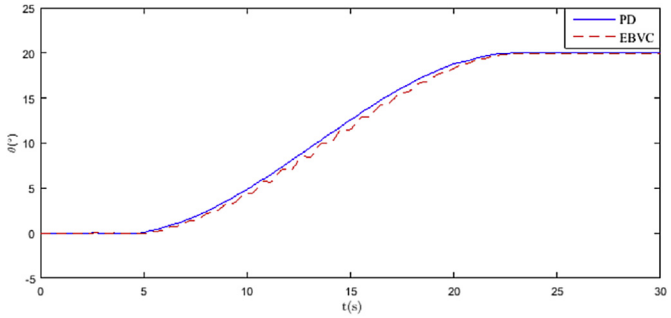

Fig. 29. The curves of the joint angle.

$$\boldsymbol{\Psi}_{t0} = [5^o \quad -5^o \quad -2.5^o]^T \tag{44}$$

The initial joint angles of the space manipulator are as follows:

$$\boldsymbol{\Theta}_0 = [5^o \quad -54^o \quad 0^o \quad 150^o \quad -5^o \quad 35^o \quad 95^o]^T \tag{45}$$

The 3D mode corresponding to the initial state of the system is shown in Fig. 18. The linear velocity of the target's CM relative to the inertial frame and the angular velocity of the chaser's base are as follows:

$$\mathbf{v}_t = [-5 \quad 5 \quad 5]^T \text{mm}/s \tag{46}$$

$$\boldsymbol{\omega}_t = [0.3 \quad 0 \quad 0]^T \ ^o/s \tag{47}$$

The control parameters used in equation (25) are:

$$\mathbf{K}_p = [80 \quad 80 \quad 20 \quad 40 \quad 2 \quad 20 \quad 0.2]^T \tag{48}$$

$$\mathbf{K}_d = [200 \quad 280 \quad 100 \quad 120 \quad 10 \quad 120 \quad 1]^T \tag{49}$$

$$\boldsymbol{\alpha} = [1.5 \times 10^6 \quad 1.5 \times 10^6 \quad 900 \quad 40 \quad 2 \quad 2 \quad 1]^T \tag{50}$$

$$\boldsymbol{\beta} = [0.1 \quad 0.1 \quad 0.1 \quad 0.1 \quad 0.1 \quad 0.1 \quad 0.1]^T \tag{51}$$

The simulation results are shown in Figs. 23–26. The y-axis component (i.e. y_G) of the end-point position (i.e. Point G shown in Fig. 19) of the solar paddle with respect to the floating coordinate system is used to describe the structure vibration. Fig. 23 shows the vibration curve of the flexible wing. From Fig. 23 we can see that the vibration is obviously reduced after using the EBVC method and the size of vibration approaches zero after 40s. The vibration level of the flexible wing by using EBVC method is significantly lower than that by using PD controller. For the PD control, the final vibration value is −23 mm. But it is only −0.02 mm for the EBVC control and satisfies the grasp condition.

Fig. 24 shows the real pose of the handle relative to the end-effector. When the end-effector approaches the target within the given thresholds of ε_p and ε_o (in this simulation, the position threshold is 0.01 m and the attitude threshold is 1°), the manipulator is commanded (at t = 49 s for PD control and t = 51.7 s for Energy-based vibration control) to capture the target. Fig. 25 depicts the curves of the manipulator joint angles. The pose of the space robot's base is shown in Fig. 26. For the PD control, the attitude and the centroid position of the base vary from $[-1.8°, -37°, 3.5°]^T$ to $[8.66°, -39.73°, -2.242°]^T$ and from [0 m, 0 m, 0 m]^T to [-0.047 m, −0.0016 m, −0.023 m]^T, respectively. And they

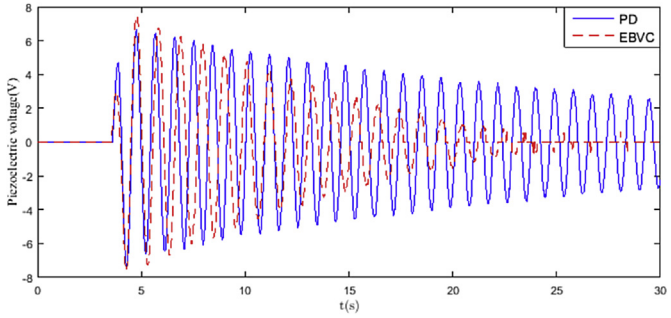

Fig. 30. Piezoelectric voltage generated by vibration of the flexible appendage.

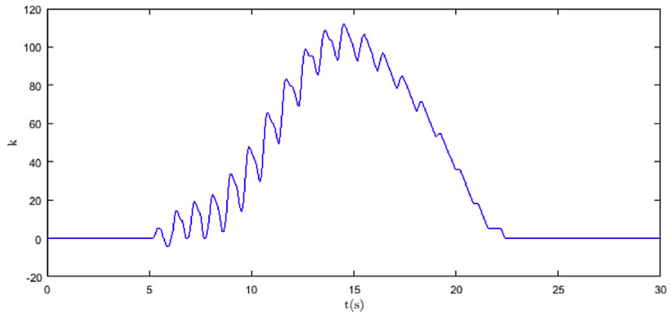

Fig. 31. The curve of k.

are respectively from [-1.8°, −37°, 3.5°]^T to [9.49°, −39.85°, −2.77°]^T and from [0 m, 0 m, 0 m]^T to [-0.049 m, −0.0022 m, −0.025 m]^T for the EBVC control. The final state of the space robot system is illustrated in Fig. 27.

All the above results show that the EBVC method significantly reduces the vibration level of flexible appendages while tracking joint trajectory with high accuracy. It is very important not only for capturing the target, but also for providing a good condition for the stability control of the compounded system after the target is grasped.

6. Experimental study

6.1. Hardware design

We design a single-degree-of-freedom space robot experimental system. The complete setup of the experiment is shown in Fig. 28. The space robot's base labelled as '1' is free-floating. The joint labelled as '2' is a revolute joint. Arm link labelled as '3' is a steel plate, which can be regarded as a rigid body. The air feet labelled as '4' supports the whole space robot system to carry out micro-friction movement. Label '5' represents the flexible appendage, which is simulated with a thin aluminium plate. The piezoelectric sensor labelled as '6' is mounted at the thin aluminium plate. The piezoelectric sensor is used to measure the size of the vibration of thin aluminium plate. Label '5' represents aluminium blocks. The power supply labelled as '8' provides 24 V voltage for the joints and the central control unit labelled as '9'. The central control unit transmits the generated control instructions to the controller of the joint. The PC labelled as '10' generates the planning trajectory and the control algorithm. The marble platform labelled as '11' provides a high-precision work plane for the air feet.

6.2. Experiment on vibration suppression of the flexible appendage

The proposed vibration suppression control of flexible appendages using the manipulator joints is verified based on the space robot experimental system. In this experiment, the joint of the manipulator moved from 0° to 20°. 3rd order polynomial function is used to plan the joint's trajectory. The total experimental time is 30s, of which the planning time is 20s. In order to make the experimental effect more obvious, we give a large initial vibration of the flexible appendage.

The experimental results are shown in Figs. 29–31. Fig. 29 shows the curves of the joint's angle. Fig. 30 shows the curve of the voltage generated by the piezoelectric sensor. The size of the voltage represents the size of the vibration of the flexible appendage. It can be seen that the speed of vibration decay of the flexible appendage by using EBVC method is significantly faster than that by using the PD controller. The vibration of the flexible appendage is substantially zero after 24 s when using EBVC method. However, when using the PD controller the piezoelectric voltage caused by the vibration of the flexible appendage is still up to 2.5 V at the end of the simulation. Fig. 31 shows the curve of the value of parameter k when using EBVC method. The value of k becomes zero when both the vibration and the joint velocity are zero.

7. Conclusion

When a space robot with flexible appendages is deployed in space, the structure flexibilities will easily cause vibration during orbit and/or attitude maneuvering of the base, and the operation of the manipulators. In this paper, we derived the rigid-flexible coupling dynamics of a space robot system with flexible appendages. Then, a method was proposed to meet the requirements of on-line trajectory planning for moving target capturing and vibration suppression control of the flexible appendages. This method is effective for the free-floating space robot with flexible appendages where the base is not actively controlled during the target capturing. In fact, it can be extended to deal with other cases, such as for target capturing using flexible-link and/or flexible-joint space robot. If the manipulator has redundancy, the disturbance on the base can be minimized. Moreover, if the attitude of the base and the manipulator joints are controlled in coordinated behaviour, the control performance will be better. In the future, we will deeply study the vibration suppression control for the above cases, i.e. flexible-joint flexible-link space robot application, optimal control based on redundancy resolution, coordinated control for high performance, and so on.

Acknowledgements

This work was supported in part by China Postdoctoral Science Foundation (grant number 2018M631473), the National Natural Science Foundation of China (grant number 61673239, 61573116, U1613227), the Natural Science Foundation of Guangdong Province (2015A030313881) and the Basic Research Program of Shenzhen (JCYJ20160301153317415, JCYJ20160301100921349, JCYJ20160428182227081).

References

[1] K. Yoshida, Engineering test satellite VII flight experiments for space robot dynamics and control: theories on laboratory test beds ten years ago, now in orbit, Int. J. Robot Res. 22 (2003) 321–335.
[2] R.B. FRIEND, Orbital express Program summary and mission overview, Proceedings of the International Society for Optical Engineering(SPIE2008), Society of Photo-Optical Instrumentation Engineers, Orlando, FL, USA, 2008695803.695801-695803.695811.
[3] K. Yoshida, Y. Umetani, Control of space manipulators with generalized Jacobian matrix, Space Robotics: Dynamics and Control, Springer, US, 1993, pp. 165–204.
[4] H. Nagamatsu, T. Kubota, I. Nakatani, Autonomous retrieval of a tumbling satellite based on predictive trajectory, IEEE International Conference on Robotics and Automation (ICRA1997), IEEE, Albuquerque, NM, USA, 1997, pp. 3074–3079.
[5] W. Xu, B. Liang, C. Li, Y. Xu, Autonomous rendezvous and robotic capturing of non-cooperative target in space, Robotica 28 (2010) 705–718.
[6] G. Dong, Z.H. Zhu, Autonomous robotic capture of non-cooperative target by adaptive extended Kalman filter based visual servo, Acta Astronaut. 122 (2016) 209–218.
[7] B.P. Larouche, Z.H. Zhu, Autonomous robotic capture of non-cooperative target using visual servoing and motion predictive control, Aut. Robots 37 (2014) 157–167.
[8] L. Chen, P. Huang, J. Cai, Z. Meng, Z. Liu, A non-cooperative target grasping position prediction model for tethered space robot, Aero. Sci. Technol. 58 (2016) 571–581.

[9] P. Huang, Z. Lu, Z. Liu, State estimation and parameter identification method for dual-rate system based on improved Kalman prediction, Int. J. Control, Automat. Syst. 14 (2016) 998–1004.
[10] P. Zarafshan, S.A.A. Moosavian, Control of a space robot with flexible members, IEEE International Conference on Robotics and Automation (ICRA2011), IEEE, Shanghai, China, 2011, pp. 2211–2216.
[11] L. Meirovitch, R. Quinn, Equations of motion for maneuvering flexible spacecraft, J. Guid. Contr. Dynam. 10 (1987) 453–465.
[12] C.T. Kiang, A. Spowage, C.K. Yoong, Review of control and sensor system of flexible manipulator, J. Intell. Rob. Syst. 77 (2015) 187–213.
[13] H. Rahimi, M. Nazemizadeh, Dynamic analysis and intelligent control techniques for flexible manipulators: a review, Adv. Robot. 28 (2014) 63–76.
[14] H. Yang, J. Liu, X. Lan, Observer design for a flexible-link manipulator with PDE model, J. Sound Vib. 341 (2015) 237–245.
[15] H. Yang, J. Liu, Distributed piezoelectric vibration control for a flexible-link manipulator based on an observer in the form of partial differential equations, J. Sound Vib. 363 (2016) 77–96.
[16] T. Yang, S. Yan, Z. Han, Nonlinear model of space manipulator joint considering time-variant stiffness and backlash, J. Sound Vib. 341 (2015) 246–259.
[17] W. Li, B. Luo, H. Huang, Active vibration control of flexible joint manipulator using input shaping and adaptive parameter auto disturbance rejection controller, J. Sound Vib. 363 (2016) 97–125.
[18] D. Hirano, Y. Fujii, S. Abiko, R. Lampariello, K. Nagaoka, K. Yoshida, Vibration suppression control of a space robot with flexible appendage based on simple dynamic model, IEEE International Conference on Intelligent Robots and Systems (IROS2013), IEEE, Tokyo, Japan, 2013, pp. 789–794.
[19] D. Hirano, Y. Fujii, S. Abiko, R. Lampariello, K. Nagaoka, K. Yoshida, Simultaneous control for end-point motion and vibration suppression of a space robot based on simple dynamic model, IEEE International Conference on Robotics and Automation (ICRA2014), IEEE, Hong Kong, China, 2014, pp. 6631–6637.
[20] H. Kojima, S. Ieda, S. Kasai, Frequency-tuning input-shaped manifold-based switching control for underactuated space robot equipped with flexible appendages, Acta Astronaut. 101 (2014) 42–54.
[21] S. Kasai, H. Kojima, Input-shaped link motion control of planar space robot equipped with flexible appendage, Trans. Jpn. Soc. Aeronaut. Space Sci. 55 (2012) 205–213.
[22] P. Gasbarri, A. Pisculli, Dynamic/control interactions between flexible orbiting space-robot during grasping, docking and post-docking manoeuvres, Acta Astronaut. 110 (2015) 225–238.
[23] P. Zarafshan, S.A.A. Moosavian, E. Papadopoulos, Adaptive hybrid suppression control of space free-flying robots with flexible appendages, Robotica (2014) 1–22.
[24] Z.-w Yu, X.-f Liu, G.-p Cai, Dynamics modeling and control of a 6-DOF space robot with flexible panels for capturing a free floating target, Acta Astronaut. 128 (2016) 560–572.
[25] W. Xu, D. Meng, Y. Chen, H. Qian, Y. Xu, Dynamics modeling and analysis of a flexible-base space robot for capturing large flexible spacecraft, Multibody Syst. Dyn. 32 (2014) 357–401.
[26] D. Meng, H. Liu, Y. Li, W. Xu, B. Liang, Vibration suppression of a large flexible spacecraft for on-orbit operation, Sci. China Inf. Sci. 60 (2017) 050203.
[27] S. Dubowsky, M.A. Torres, Path planning for space manipulators to minimize spacecraft attitude disturbances, IEEE International Conference on Robotics and Automation (ICRA1991), IEEE, 1991, pp. 2522–2528.
[28] M.A. Torres, Modeling, Path-planning and Control of Space Manipulators: the Coupling Map Concept, Massachusetts Institute of Technology, 1993.
[29] M. Bergerman, C. Lee, Y. Xu, A dynamic coupling index for underactuated manipulators, J. Rob. Syst. 12 (1995) 693–707.
[30] Y. Xu, H.Y. Shum, Dynamic control and coupling of a free-flying space robot system, J. Rob. Syst. 11 (1994) 573–589.
[31] D. Meng, X. Wang, W. Xu, B. Liang, Space robots with flexible appendages: dynamic modeling, coupling measurement, and vibration suppression, J. Sound Vib. 396 (2017) 30–50.
[32] D. Meng, B. Liang, W. Xu, X. Wang, H. Liu, X. Zhu, On the autonomous target capturing of flexible-base space robotic system, 13th International Conference on Control Automation Robotics & Vision (ICARCV2014), IEEE, Marina Bay Sands, Singapore, 2014, pp. 1894–1899.
[33] Y. Umetani, K. Yoshida, Resolved motion rate control of space manipulators with generalized Jacobian matrix, IEEE Trans. Robot. Autom. 5 (1989) 303–314.
[34] S. Chiaverini, B. Siciliano, O. Egeland, Review of the damped least-squares inverse kinematics with experiments on an industrial robot manipulator, IEEE Trans. Contr. Syst. Technol. 2 (1994) 123–134.
[35] A. Trevisani, M.E. Valcher, An energy-based adaptive control design technique for multibody-mechanisms with flexible links, IEEE-ASME T. Mech 10 (2005) 571–580.
[36] T. Lee, S. Ge, Z. Wang, Adaptive robust controller design for multi-link flexible robots, Mechatronics 11 (2001) 951–967.